Engineering Analysis with Boundary Elements 116 (2020) 14–30

Contents lists available at ScienceDirect

Engineering Analysis with Boundary Elements

journal homepage: www.elsevier.com/locate/enganabound

A binary-tree element subdivision method for evaluation of singular domain integrals with continuous or discontinuous kernel

Jianming Zhang [a,*], Baotao Chi [a], Krishna M. Singh [b], Yudong Zhong [a], Chuanming Ju [a]

[a] State Key Laboratory of Advanced Design and Manufacturing for Vehicle Body, College of Mechanical and Vehicle Engineering, Hunan University, Changsha 410082, China

[b] Department of Mechanical and Industrial Engineering, Indian Institute of Technology, Roorkee, India

ARTICLE INFO

Keywords:
BEM
Singular domain integral
Continuous kernel
Discontinuous kernel
Gaussian quadrature
Hammer–Stroud quadrature

ABSTRACT

A novel element subdivision method based on the binary tree has been proposed for evaluation of singular domain integrals in BEM. In this paper, this element subdivision technique is called the Binary-Tree Subdivision Method (BTSM), which is applicable to arbitrary shape linear and curved volume elements with arbitrary locations of the source point. Compared to the Conventional Subdivision Method (CSM), a significant advantage of the BTSM is that it can handle singular domain integrals with continuous or discontinuous kernel and improve the accuracy of integration even with distorted elements. With the distinct feature that a single binary-tree data structure can efficiently handle volume element subdivision, it is flexible and convenient for the BTSM to be implemented in the formulation of the boundary integral equation which contains volume integrals. In addition, for the volume integrals with discontinuous kernel, an improved general projection algorithm based on Newton iteration has been proposed for curved boundary matching. Experiment results have demonstrated that the volume element is always subdivided by the BTSM in a fully automated manner and high-quality patch generation can be guaranteed in any situation. Several examples are given to verify the validity, robustness and accuracy of the proposed method.

1. Introduction

With the distinct advantage that boundary integral formulations have the ability to reduce the dimensionality of the linear and exterior problems, the boundary element method (BEM) [1] has made considerable achievements in many fields with both academic and engineering applications, such as potential problems [2,3], elastostatic problems [4–6], fracture mechanics problems [7,8] and acoustics problems [9,10]. However, the pure boundary integral formulations are not available in general. Owing to the absence of the fundamental solutions in general nonlinear problems and problems in non-homogeneous media, the fundamental solutions of simplified operators can be used with resulting into the so-called boundary-domain formulations. In the presence of body forces, time dependent effects or certain class of nonlinearities, the resultant integral equation generally contains volume integrals, such as the transient heat conduction problems [11], elastodynamic problems [12], elasto-plastic problems [13], etc. Then, the specific domain of the original problem is generally required to be discretized into internal cells because of unknown field variables involved in domain integral integrands. How to accurately evaluate the volume integrals has always been attracted much attention in the BEM community.

In the efforts to improve the performance of the evaluation of volume integrals, various numerical methods have been developed and achieved considerable progress in BEM [14]. These methods for the treatment of volume integrals are categorized into two main schemes: (i) converting the volume integrals into boundary ones and some non-integral terms, (ii) computing the volume integrals directly. The first way is concerned with conversion of the volume integral into a boundary counterpart by combining with various integral transformation techniques. In order to avoid the use of the domain discretizetion, the dual reciprocity method (DRM) has been coupled successfully to boundary integral formulations, which is an approximate form of the particular integral approach by employing the boundary discretization and the radial basis function. As has been demonstrated in [15], some internal points should be considered in the DRM. The location of internal points can be selected arbitrarily, but the shape or basis functions used for interpolation in the domain are not arbitrary. These functions should have particular solutions and they cannot be selected arbitrarily. It is worth mentioning that the accuracy and efficiency of the DRM is more sensitive to the distribution and loca-

* Corresponding author.
E-mail address: zhangjm@hnu.edu.cn (J. Zhang).

https://doi.org/10.1016/j.enganabound.2020.03.023
Received 3 July 2019; Received in revised form 16 January 2020; Accepted 25 March 2020
Available online 11 April 2020

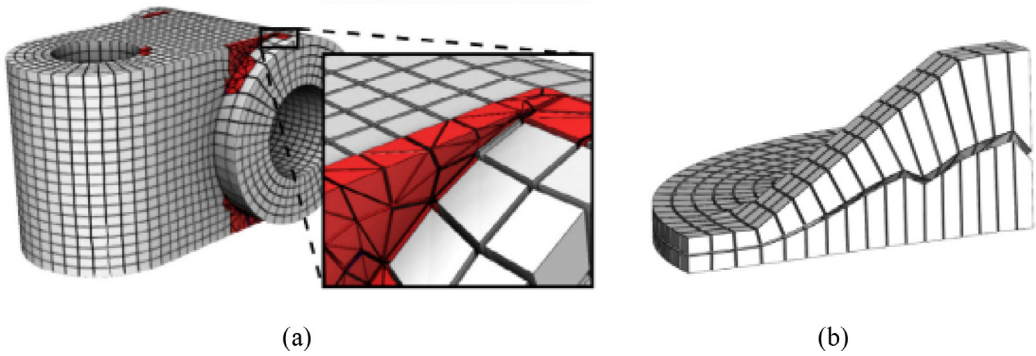

Fig. 1. Adaptive mesh generation of mechanical CAD models: (a) irregular tetrahedral element, (b) all-hexahedral mesh.

tion of the domain points employed to approximate the source term. A key difficulty for better distribution of the domain points is that it relies on a fine domain mesh for distributing the domain points. In addition, the radial integration method (RIM) [16] is another effective technique for evaluating the volume integrals with boundary-only discretization, in which the volume integral is converted into an equivalent boundary integral through the use of straight-path integrals emanating from the source point. On the other hand, another way is to compute the volume integrals directly with the domain discretizetion. The conventional direct volume integration method (DVIM) was significantly better than the DRM, which has been demonstrated numerically in [17]. Recently, some successful improved methods for evaluation of volume integrals based on the DVIM have been developed and implemented in the 3D transient heat conduction problem [18]. Dong et al. [19] proposed a coordinate transformation method called the (α, β, γ) transformation, which can be employed in the pyramidal patches for computation of volume integrals.

The FEM and BEM both have made great achievements and achieved remarkable progress in many fields with both academic and industrial applications. The BTSM is both applicable to BEM and FEM. Due to the existence of singularity in BEM, the BTSM is primarily proposed to evaluate the singular domain integrals in boundary integral formulations. Owing to the absence of the fundamental solutions in BEM, the value of the integrand varies precipitously around the source point. Whereas, there is no singularity in the domain integrals of FEM in general. In order to evaluate the singular domain integrals accurately, numerical results obtained in BEM through the use of more integration points than that in FEM. Thus, the BTSM for FEM is more efficient than those for BEM. In FEM, application of the X-FEM to solve the fracture mechanics problems [20], singular shape functions are generally introduced to smooth the singularity of the stress field at the crack tip. The BTSM is convenient and applicable to evaluate this type of volume integrals in X-FEM. To evaluate this type of volume integrals in X-FEM is also an extremely important research issue. Moreover, an attractive key advantage of the BTSM is that it can be both applicable to evaluate the volume integrals for continuous and discontinuous elements. Note that the trial functions are required to maintain at least C^0 continuity in FEM, which is not required for the BEM. One of the remarkable features between BEM and FEM is that both continuous and discontinuous elements can be applied in BEM. Discontinuous grids can provide more convenience for mesh generation without considering the hanging points for its simplicity in dealing with complex geometries.

Another important and attractive topic in the computational field of BEM is to reduce the sensitivity of the integration results to the mesh distortions. Nevertheless, it remains a challenging task to create a desirable mesh automatically in real applications. Note that a key difficulty in mesh generation is to meet the connectivity requirements of the desirable mesh without any hanging points, which causes a great deal of work for automatic meshing, such as the Delaunay triangulation-based approach, the advancing-front-technique-based approach, the grid-based method, the all-hexahedral mesh algorithm, and so forth. In addition, a broad consensus has emerged in BEM that automatic mesh generation is still a bottleneck for complex geometries and high performance computing in structural engineering. The quality of the resulting mesh generation is crucial to the evaluation of volume integrals. However, distorted or irregular elements are probably unavoidable in the process of automatic meshing (see Fig. 1), which may result in the domain discretizations with inferior approximation properties. An immediate consequence of mesh distortion is leading to inaccurate or even invalid computational analyses, especially for the integration in the BEM implementation. Thus, accurate evaluation of the volume integrals with distorted or irregular elements is a very significant research subject to investigate in BEM.

In view of the direct computation method of the volume integrals, each volume element is usually required to be subdivided into several standard patches for which a established rule of the integration is available, then the numerical integration can be computed in the given patch. Up to now, the main widely used element subdivision techniques are the Conventional Subdivision Method (CSM) [21] (Fig. 2(a)), the Quad-Tree Subdivision Method (QTSM) [22] (Fig. 2(b)), the Spherical Subdivision Method (SSM) [23] (Fig. 2(c)) and other methods, but unfortunately, none of them are perfect in terms of accuracy or robustness. Many of these methods generate the hexahedral patches, the pentahedral patches, the tetrahedral patches and the pyramid patches on the entire element directly. For some irregular elements, lower quality or even degenerated patches may be obtained by using the CSM or the QTSM. The QTSM produces significant amounts of pleonastic patches for integration through the use of the quad-tree data structure, which leads to the complexity of calculation increasing. The SSM is a type of three-dimensional advancing front technique by a sequence of spheres of different sizes applied to volume element subdivision. Although the SSM has been succeeded in overcoming the difficulties related to the integration in BEM, it relies on a large quantity of segmentation templates and cannot guarantee successful element subdivision for some situations.

In this paper, a new element subdivision method for evaluation of the singular domain integrals is proposed, which is mainly based on the new binary-tree data structure [24] and various cavity projection algorithms. The contributions of the BTSM can be summarized in five aspects: (i) A scheme of the BTSM is proposed to evaluate singular domain integrals with continuous or discontinuous kernels. (ii) The BTSM is applicable to linear and curved volume elements of arbitrary shape and automatic high-quality patch generation can be guaranteed under any circumstances. (iii) The BTSM is both applicable to evaluate the volume integrals for continuous and discontinuous elements. (iv) Even with the distorted or irregular volume elements, the BTSM can exhibit high accuracy and excellent robustness behavior. (v) The current approach is more convenient and invariably achievable to implement without any

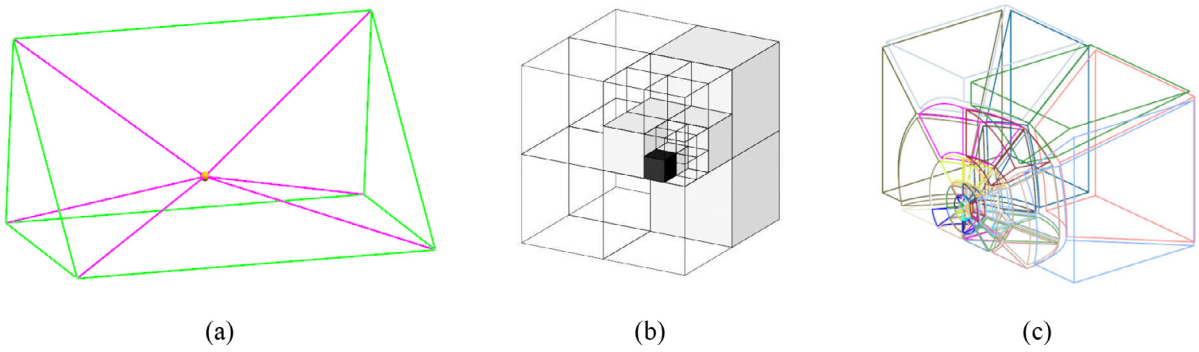

Fig. 2. Various element subdivision methods for singular domain integrals: (a) conventional subdivision method, (b) quad-tree subdivision method, (c) spherical element subdivision method.

segmentation templates by the single binary-tree data structure and the cavity projection algorithms.

This paper is organized as follows. Section 2 describes the main ideas of the BTSM for singular domain integrals with continuous or discontinuous kernel. Section 3 introduces the binary-tree subdivision scheme for volume elements with arbitrary shape. Construction of many different types of the valid core cavities for various situations is discussed Section 4. Detailed description of the cavity projection algorithms for both linear and curved volume elements are presented in Section 5. Numerical results for different kinds of volume elements with various positions of the source point are shown in Section 6 and conclusions are given in Section 7.

2. Overview of the BTSM for singular domain integrals

In BEM formulations, the integrands of the volume integrals are generally classified into two primary kinds: continuous function and discontinuous function. A graphical illustration of the integrand of the volume integrals is provided in Fig. 3. Singular domain integrals arise when the point locates inside or directly on the boundary of element. If the integrand of the volume integrals is infinite at some points, the integral is singular. For the transient heat conduction problem based on the time-dependent fundamental solution, while the integral kernel is a regular continuous function everywhere defined on the domain Ω, the value of the integrand varies precipitously around the source point or when a small time step is used. For the fundamental solution of elastodynamic problems and electromagnetic field analysis, the integral kernel is discontinuous at some points (denoted as the discontinuous points), it is unavailable to evaluate the volume integrals accurately using a straightforward calculation based on the classical Gaussian quadrature or Hammer–Stroud quadrature [25]. Consider an arbitrary domain Ω, the volume integral involved in the three-dimensional problems can be expressed as

$$I(P) = \int_{\Omega} f(P,Q)(WQ)d\Omega \tag{1}$$

where the notations P and Q are the source point and the field point in Ω, respectively. The functions $f(P, Q)$ and $W(Q)$ are respectively the integral kernel and the arbitrary distributed function. Unless otherwise mentioned, the non-mesh source points mainly refer to the nodes in the continuous and discontinuous elements in BEM.

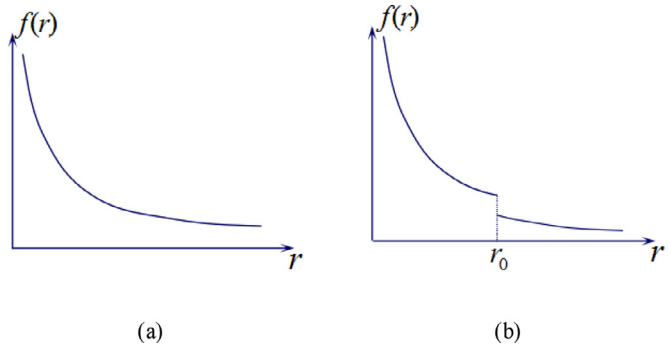

Fig. 3. The integrand of the volume integrals: (a) the continuous function, (b) the discontinuous function.

In numerical simulation, the physical space is discretized into small volumes and the partial differential equations integrated over each of these volume elements. The initial volume elements in BTSM primarily refer to the unstructured meshes, such as the hexahedral, pentahedral and tetrahedral elements. For each prescribed volume element, the BTSM is then subdivided in the local coordinate system of the element. To illustrate the BTSM more clearly, the main ideas of this method for evaluating singular domain integrals are graphically illustrated in Fig. 4 in two dimensions. The BTSM implementation for singular domain integrals is a generalization of the algorithm for the two-dimensional case. As is shown in Fig. 5, the algorithm of the BTSM takes a hexahedral element from the thin sections of a 3-D solid model as the input and outputs the ultimate well-shaped patches result automatically, and it mainly involves the following four steps. The first step is determination of the subdivision parameters (the subdivision ratio and the minimum subdivision size) for the prescribed volume element and relative position of the source point. Then, the binary-tree subdivision scheme for automatic volume element subdivision is executed, which includes the volume element subdivision rules, a new type of the binary-tree data structure and the volume element subdivision techniques. Next, the valid core cavities for projection, which are depicted with a group of purple lines in Fig. 4, are required to be constructed by removing all the undesired sub-elements including the interior sub-elements and the straddling sub-elements. The final step is to match the core projection cavities in an out-inside manner through the cavity faces projection process. To match the core cavities to the characteristic boundary of the sphere for high-quality patches generation, two comprehensive techniques are employed: a radial cavity projection algorithm and a general cavity projection algorithm. For curved volume elements, an improved general cavity projection algorithm based on Newton iteration for matching the target projection points on the curved boundary of element is also proposed.

In order to eliminate the singularity of the volume integrals, the ultimate patches around the source point are required to pass through it. For the volume integrals with continuous kernel, a sphere with a smaller radius that is adopted to generate serendipity patches, in which the sphere is enclosed by the boundary of volume element to avoid dealing with various complicated situations. For the volume integrals with discontinuous kernel, the specific domain is naturally divided into two sub-regions for integration by a sphere with a radius of r_0 based on

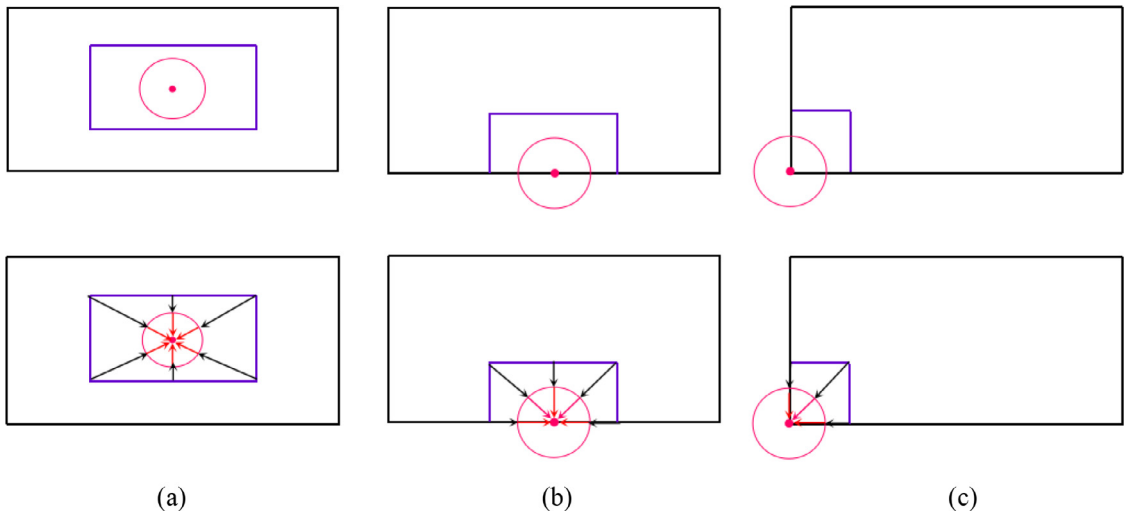

Fig. 4. The main ideas of the BTSM with arbitrary locations of the source point: (a) inside, (b) on the boundary, and (c) at vertices.

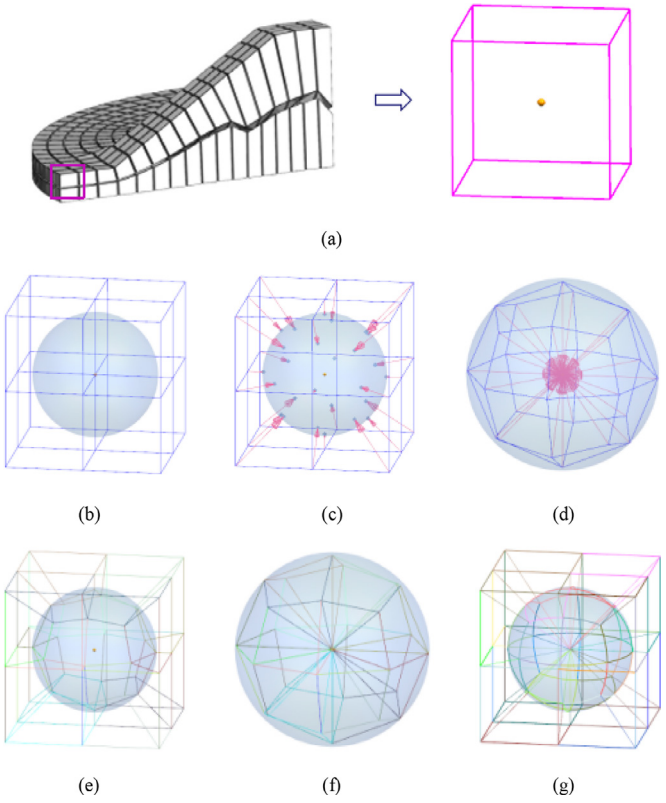

Fig. 5. Overall procedure of the patch generation process based on the BTSM: (a) a hexahedral element from the thin sections of a 3-D solid model, (b) ultimate refinement structure, (c) the outer cavity construction and relative projection points, (d) the inner cavity construction and relative projection points, (e) (f) the high-quality projection sub-elements, (g) the resulting patch generation.

its discontinuities. Here, the radius r_0 named the characteristic radius, which represents the distance from the source point to the discontinuous point. The differences between the evaluation of singular domain integrals with continuous and discontinuous kernel in the BTSM implementation, are fully discussed in the valid core projection cavities construction algorithm and the projection algorithm for matching the core cavities to the characteristic boundary of the sphere.

3. The binary-tree subdivision scheme

We provide an outline of the binary-tree subdivision scheme which includes the element subdivision criterions, details of tree data structure and adaptive refinement techniques.

3.1. Element subdivision criterions

The binary-tree subdivision scheme is similar to other spatial decomposition methods, which was originally used to approximate the geometric shape of arbitrary complicated solid model. One of the remarkable features of this approach is that automatic element subdivision can be flexibly achieved due to the characteristics of the binary tree-based level structure in recursive decomposition. In the BTSM implementation, the initial root node is similar in shape to the original volume element and it obviously can be subdivided into two children sub-elements. Each sub-element is then examined by the element subdivision criterion to determine whether further decomposition is required to be executed. The decomposition process is recursively continued until all remaining sub-elements meet the specific subdivision criterion. It should be noted that the element subdivision criterion for singular domain integrals is different from that for nearly singular domain integrals. As is depicted in Fig. 6, the element subdivision criterion is graphically explained by the two-dimensional and three-dimensional schematic descriptions, respectively.

For singular domain integrals, the element subdivision criterions are based on both the subdivision ratio η and the minimum subdivision size ε. The subdivision ratio η is defined as the ratio of circumradius l of sub-element to the distance d between the source point P and geometric center O of sub-element, i.e. $\eta = l/d$. The minimum subdivision size ε is used to avoid the infinite loop and the propagation problem of refinement patches around the source point can be controlled effectively. The subdivision criteria of the binary-tree subdivision scheme for singular domain integrals are given by (1) $\eta < \eta_{Ref}$, (2) $l < \varepsilon$. As has been demonstrated in [26], the reference subdivision ratio η_{Ref} is set to about 1.0 in general. For the volume integrals with discontinuous kernel, the minimum subdivision size ε is equal to the characteristic radius r_0. For the volume integrals with continuous kernel, the sphere with a minor radius ε is taken, which is entirely surrounded by the boundary of prescribed volume element. The parameter ε is α times of the characteristic radius R_t, i.e. $\varepsilon=\alpha R_t$, where $\alpha = 0.6 \sim 0.8$. A schematic description of related parameters of the characteristic radius R_t is graphically depicted in Fig. 6(c). The parameters d_1, d_2, d_3 denote the minimum distances from the source point P to the boundary vertices, edges, faces of the given el-

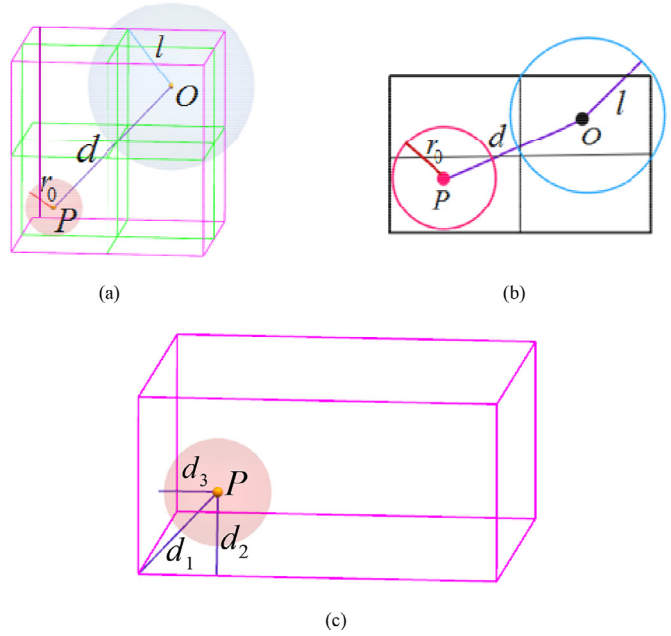

Fig. 6. The element subdivision criterion: (a) a three-dimensional graphical illustration of the subdivision criterion, (b) a two-dimensional schematic of the subdivision criterion, (c) schematic of the minimum distances from the source point to the boundary vertices, edges, faces of element.

ement, respectively. The characteristic radius R_t is the minimum value of these three parameters, i.e. $R_t = \min(d_1,d_2,d_3)$. The volume element is divided into a certain number of children sub-elements after levels of full-refinement according to the subdivision criterion. Then the generated core element subdivision structure is established. Flowchart in Fig. 7 elaborates the binary-tree subdivision scheme for singular domain integrals.

3.2. A new type of data structure for binary-tree element subdivision

A new type of the binary-tree data structure for volume element subdivision is employed in the BTSM for evaluation of singular domain integrals. Each binary-tree data structure contains the following groups of nodes:

- Root node: the topmost node in the binary tree-based level structure, which is the starting node for the conduction of other later operations;
- Internal nodes: each internal node has a parent and at least one child;
- Leaf nodes: each leaf node only has a parent without any children.

The binary-tree data structure for volume element subdivision is made up of edges, faces and bodies of sub-elements. Similarly, each binary tree for edges, faces and bodies of sub-elements has a group of nodes, in which each node has a value and a list of references to other nodes. It should be noted that there is a distinction between the binary tree for faces and the binary tree for edges or bodies of sub-elements. The conventional face-tree data structure is not suitable for volume element subdivision, which is restricted by the conformity requirements of the children faces on both sides of their parent face in the conventional binary tree data structure. The binary-tree subdivision scheme cannot be conducted continuously with the conventional face-tree data structure. However, the conformity requirement for faces of sub-elements is unnecessary during the volume element subdivision. Hence, a new type of face-tree data structure is proposed for volume element subdivision. As is illustrated in Fig. 8, the children faces on both sides of their parent face can be different, which are named the independent twin children faces in the face-tree data structure. Since there are no gaps between the

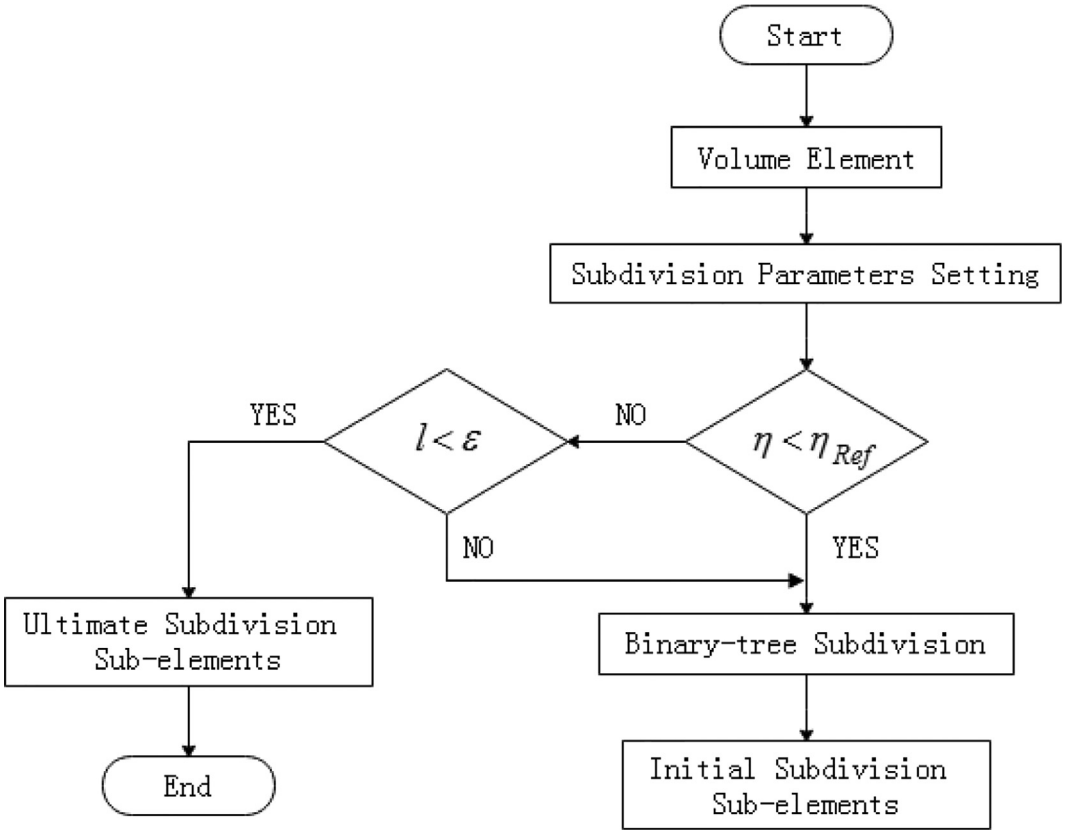

Fig. 7. Flow diagram of the binary-tree subdivision scheme.

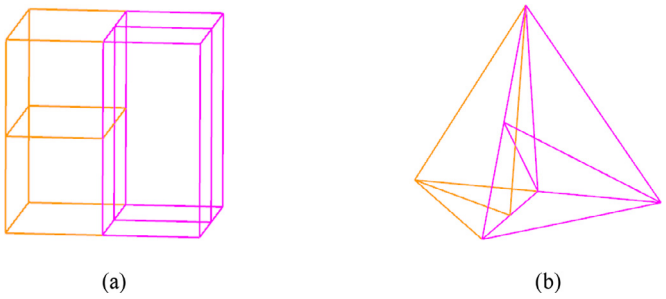

Fig. 8. Schematic of the children faces between adjacent sub-elements: (a) a quadrilateral face tree node, (b) a triangular face tree node.

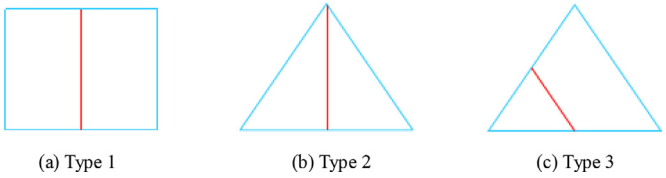

Fig. 9. Three basic types of face configuration for the face-tree data structure. (a) Type 1 (b) Type 2 (c) Type 3.

independent twin children faces of adjacent sub-elements in the local coordinate system, it will not affect the calculation of singular domain integrals.

In the process of recursive element subdivision, each face of the sub-element can be subdivided into two same or different sub-faces on its both sides according to the split direction. As is depicted in Fig. 9, three basic types of face configurations are established based on various volume element subdivision techniques. These face configurations can be classified into two categories. The first category has only one way of the decomposition for quadrilateral faces; that is, quadrilateral decomposition is carried out by dividing the quadrilateral face in the central direction (see Type 1). The second category has two possible subdivisions of a triangular face, including Types 2 and 3. Type 2 indicates that a triangular face can be subdivided into two equal-sized children faces. Type 3 represents that the triangular decomposition can be conducted by splitting the triangular face into a triangular children face and a quadrilateral children face. Combined with these face configuration techniques, it is flexible and convenient for the BTSM to handle arbitrary volume element subdivision in a fully automated manner.

3.3. Adaptive refinement techniques

The variety of the volume elements includes hexahedral elements, pentahedral elements and tetrahedral elements. A set of adaptive refinement techniques in Fig. 10 is created to achieve the best qualified

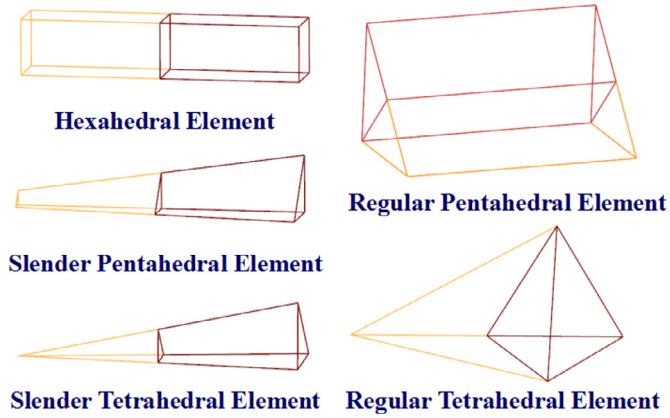

Fig. 10. A set of adaptive refinement templates.

subdivision based on the geometric features of the prescribed volume element. A hexahedral element can be subdivided into two equal-sized hexahedral sub-elements. The decomposition of a slender pentahedral element is carried out by dividing all round the slender quadrilateral faces and produces two pentahedral sub-elements. Similarly, the decomposition of a slender tetrahedral element is conducted by dividing all round the slender triangular faces and generates two tetrahedral sub-elements. For a regular pentahedral element, the decomposition is carried out by dividing both the top and bottom triangular faces along the midline and produces two pentahedral sub-elements. For a regular tetrahedral element, the decomposition is carried out by dividing two adjacent triangular faces along the midline and generates two tetrahedral sub-elements. It should be noted that the BTSM is implemented by the local coordinate system; that is, there is no need to employ any templates for the harmonious transition between the sub-elements in refinement regions and those in non-refinement regions. With the addition of these adaptive refinement techniques, several examples for different types of volume elements in Fig. 11 graphically demonstrate the feasibility and advantages of the binary-tree subdivision scheme.

4. Construction of the jagged core projection cavity

Section 4 illustrates the overall procedure of the valid projection cavities construction process. Detailed description of the jagged core cavity construction algorithm is described in Section 4.1. For the volume integrals with discontinuous kernel, if the sphere with larger radius that intersect with the boundary of volume element, the point insertion algorithm for inner cavity construction is proposed in Section 4.2.

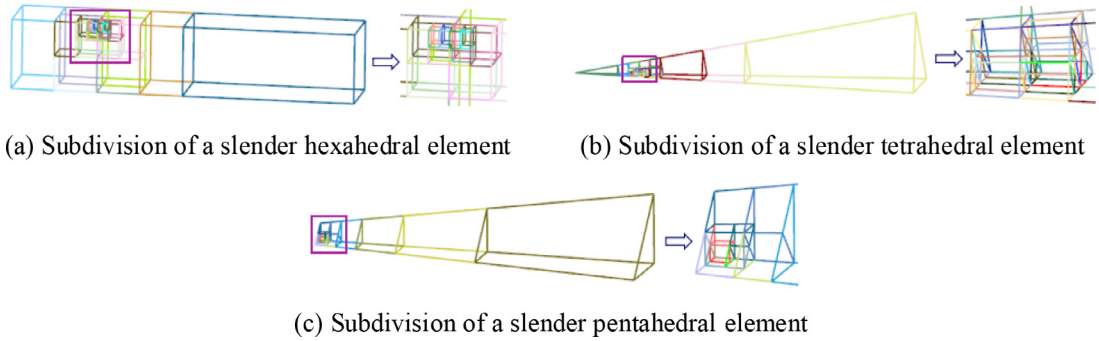

Fig. 11. Several examples of the binary-tree subdivision scheme. (a) Subdivision of a slender hexahedral element . (b) Subdivision of a slender tetrahedral element. (c) Subdivision of a slender pentahedral element.

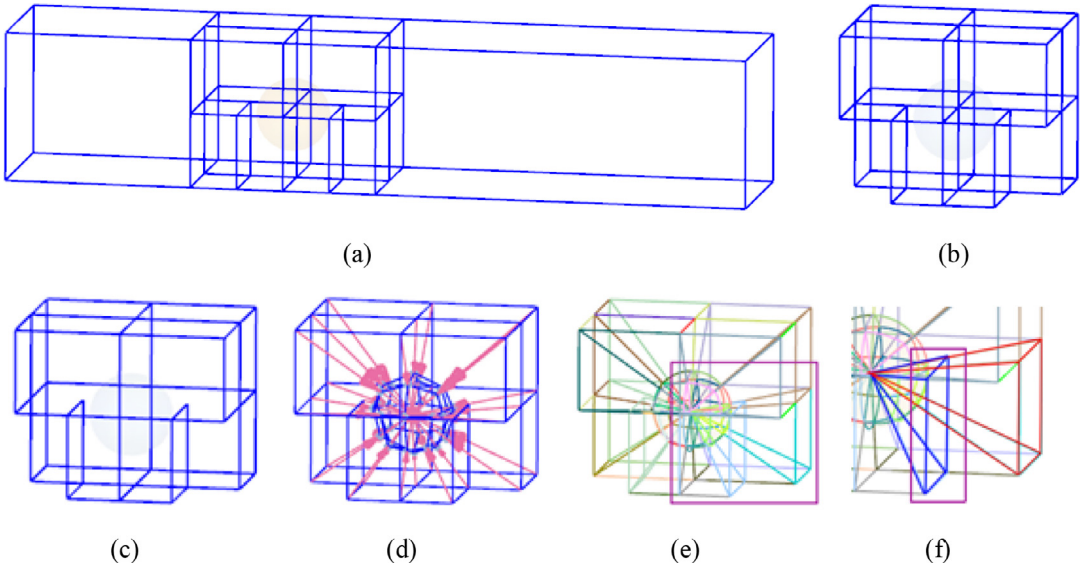

Fig. 12. Overall procedure of the invalid jagged core projection cavity construction: (a) ultimate refinement structure, (b) the straddling sub-elements, (c) (d) the invalid outer cavity construction and relative projection points, (e) the patches around the sphere with projection interference, (f) the partial enlarged view of the projection interference.

4.1. The jagged core cavity construction algorithm

In order to eliminate the singularity of the volume integrals, the patches around the source point are required to pass through it. Construction of the valid jagged core projection cavities is an indispensable part for ultimate patch generation. This process is carried out through undesired sub-elements elimination and free face extraction. The jagged core refinement structure is generated by eliminating the sub-elements that are not entirely in the exterior of the sphere. The faces of the sub-elements are divided into two groups by the number of attached elements, viz., singly defined and doubly defined faces [27]. The singly defined and doubly defined faces are recognized as free and interior faces, respectively. In this way, free faces of the straddling sub-elements that bonded with the exterior sub-elements can be easily extracted and collected to construct the outer projection cavity. However, there is a surface-gap between the outer projection cavity and the spherical surface. A layer of new patches named outer projection patches are required to be generated to fill the surface-gap by projecting the faces of the outer projection cavity. Then, free faces of the outer projection patches are taken as the components of the inner cavity. The new patches named inner projection patches are further created by directly connecting the source point and corresponding points on the inner cavity faces. The resulting patch generation after filling the surface-gap and the void spaces of the sphere is shown in Fig. 13(f).

Since the characteristic of non-conformity between the sub-elements in the refinement structure, it might not be acceptable for the valid jagged core projection cavities construction. The sub-elements in the vicinity of spherical surface are fully refined with different levels. As such, the continuity of the cavity faces cannot be ensured, which leads to the projection interference between outer projection patches (see Fig. 12(e)). In this situation, the sub-elements around the spherical surface whose one edge is a straddling node, are required to be balanced in the same level. As is shown in Fig. 13, valid jagged core projection cavities can be constructed for inner and outer projection patches generation based on the balanced process.

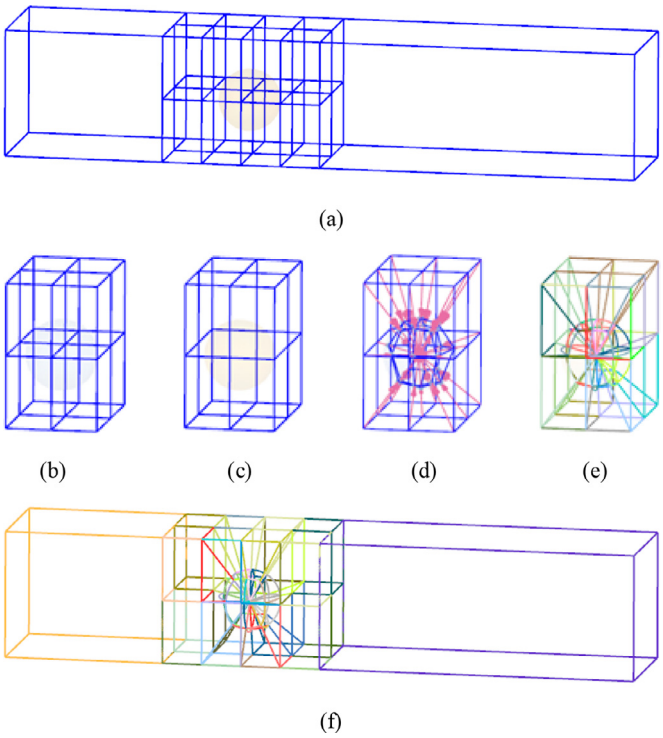

Fig. 13. Overall procedure of the valid jagged core projection cavities construction: (a) the balanced refinement structure, (b) the straddling sub-elements, (c) the valid projection cavity construction, (d) the projection cavities and relative projection points, (e) the high-quality projection sub-elements around the sphere, (f) the resulting patch generation.

4.2. The point insertion algorithm for cavity construction

Construction of the outer projection cavity is followed by the removal process of interior sub-elements and straddling sub-elements. This removal process is conducted by enclosing the spherical surface and taking regular faces as the cavity faces. For the volume integrals with discontinuous kernel, the sphere intersects the boundary of volume element if a larger radius is taken. It is unenforceable to construct any enclosing outer projection cavity only by regular faces in some cases. An adaptive virtual cavity face zoning algorithm has been successfully implemented for the valid outer projection cavity construction. Fig. 14

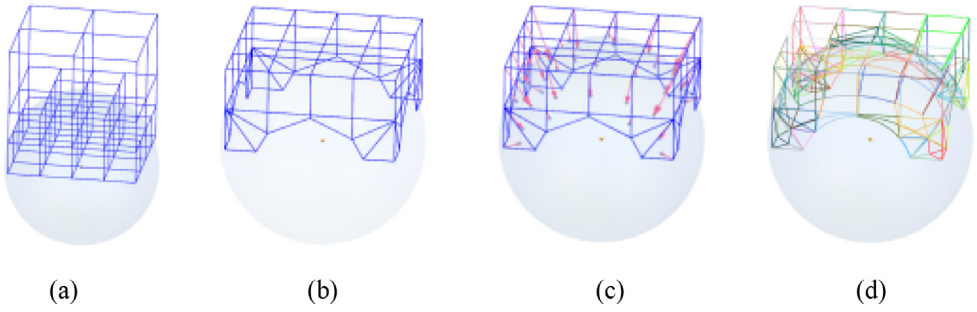

Fig. 14. Schematic of the virtual cavity face zoning algorithm for outer cavity construction: (a) ultimate refinement structure, (b) the outer cavity construction, (c) relative projection points, (d) the high-quality projection sub-elements around the sphere.

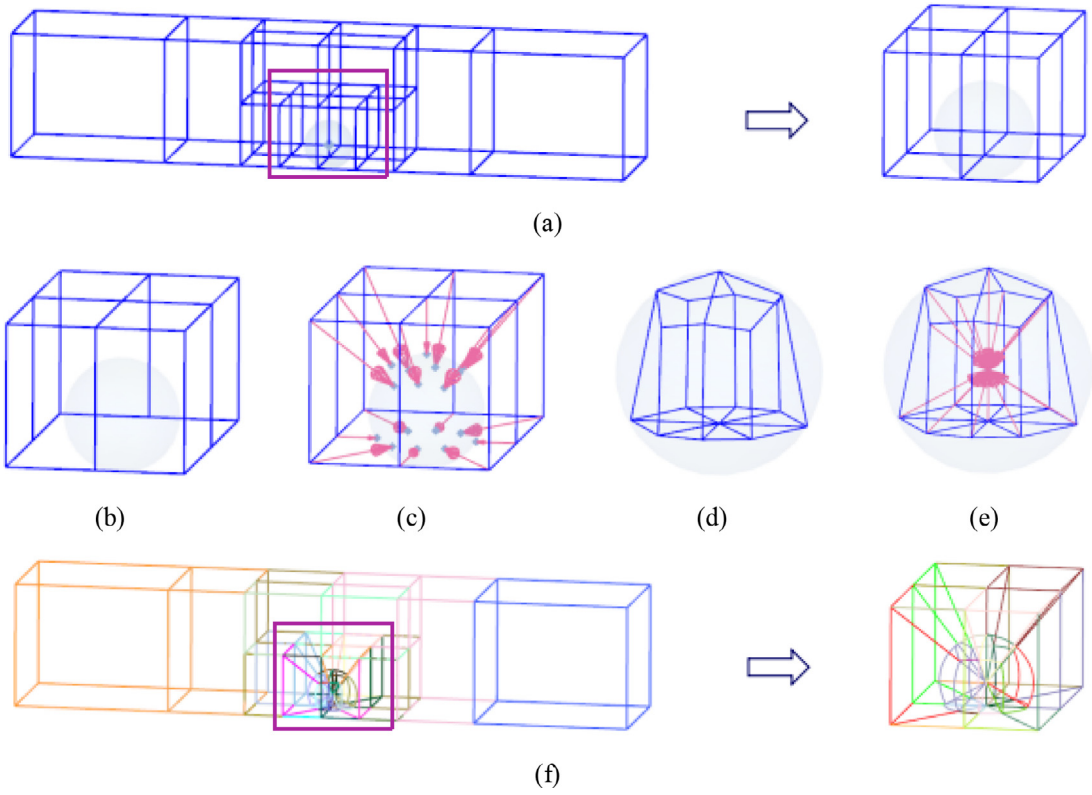

Fig. 15. Overall procedure of the point insertion algorithm for inner cavity construction: (a) the balanced refinement structure and the straddling sub-elements, (b)(c) the outer projection cavity and relative projection points, (d)(e) the inner projection cavity and relative projection points, (f) the resulting patch generation.

shows the procedure of the outer projection cavity construction process using the virtual cavity face zoning algorithm. More details of this algorithm can be available in [26]. In addition, the interior boundary intersection parts are also considered as the components of the inner projection cavity. However, due to the complexity of the intersection between the spherical surface and the boundary of element, the interior boundary intersection part is usually a polygon region on each root face. The point insertion algorithm for inner cavity construction is proposed to decompose the polygon region into regular cavity faces.

The point insertion algorithm for inner cavity construction is carried out through the following techniques (see Fig. 15):

(1) Construct the valid outer projection cavity and generate outer projection patches for boundary matching;
(2) Collect the projection points of the outer projection cavity faces and form the interior boundary intersection polygons on each root face;
(3) Compute the center of every polygon region and insert a center point in the polygon loop;
(4) By directly connecting the center point and the projection points in the polygon loop, triangulation of an arbitrary set of points can be constructed in a purely sequential manner;
(5) Pick up the free faces of the outer projection patches and triangular faces in the interior boundary intersection region as the components of the inner cavity.

5. Boundary matching of the projection cavity

More implementation details of the boundary matching of the projection cavities will be given in this section. Two comprehensive techniques are employed to match the core projection cavities to the characteristic boundary of sphere, i.e., the radial cavity projection algorithm and the improved general cavity projection algorithm. For curved volume elements, an improved general cavity projection algorithm based on Newton iteration for matching the target projection points on the curved boundary of element is also proposed.

5.1. The radial cavity projection algorithm

Since the jagged core projection cavities from the previous steps are composed of rugged shaped faces of sub-elements that do not follow the shape of the spherical surface, every point on the projection cavity faces is enforced to move to the characteristic boundary of sphere. If

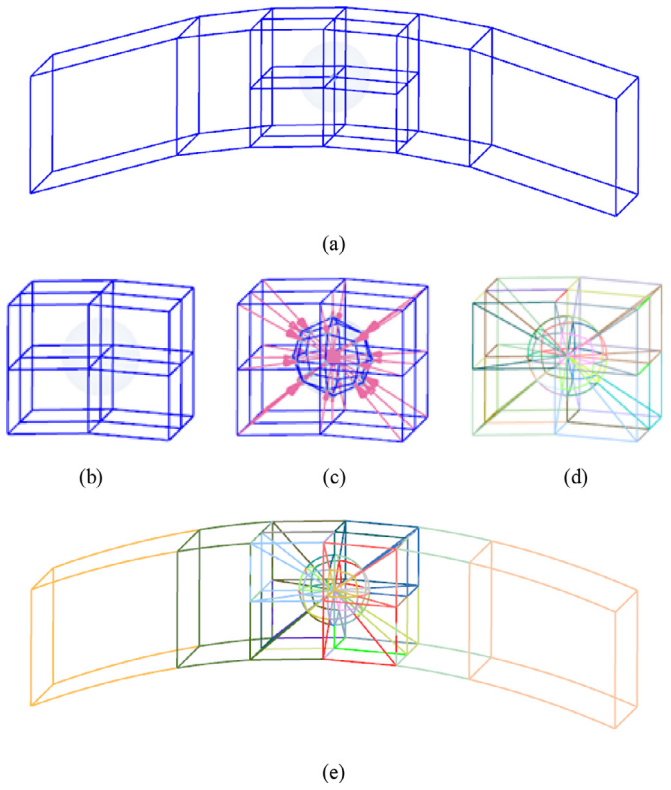

Fig. 16. Overall procedure of the radial cavity projection algorithm for projection: (a) ultimate refinement structure, (b) the straddling sub-elements, (c) the valid projection cavities and relative projection points, (d) the high-quality projection sub-elements around the sphere, (e) the resulting patch generation.

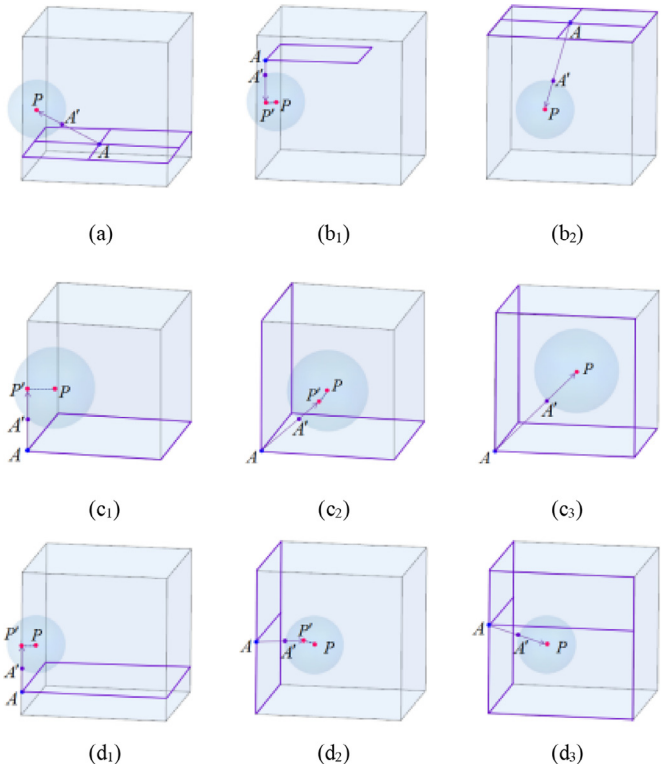

Fig. 17. Schematic of the improved general projection algorithm: (a) projection of the interior point, (b_1) projection of the boundary point whose adjacent cavity faces do not locate on any root face, (b_2) projection of the boundary point that belongs to multiple boundary cavity faces, (c_1)(c_2)(c_3) projection of the corner point whose adjacent cavity faces belong to one, two or three root faces, respectively, (d_1) projection of the frame point whose adjacent cavity faces do not locate on any root face, (d_2)(d_3) projection of the frame point whose adjacent cavity faces belong to a single or two root faces, respectively.

a smaller radius of the sphere is taken, the boundary of spherical surface is entirely surrounded by the outer and inner projection cavities. As mentioned, the projection cavities are composed of triangular or quadrilateral faces. New patches are generated layer by layer by projecting the cavity faces along the radial direction to fill the surface-gap and the interior void spaces. As is shown in Fig. 16, the newly generated patches around the spherical surface can be classified into hexahedral, pentahedral, tetrahedral or pyramidal patches. In the BTSM implementation, we adopt the classical Gauss quadrature for hexahedral and pyramid patches. The Hammer–Stroud quadrature rules are employed for the integration of tetrahedral patches. More details of the proper quadrature rules for symplectic domains can be available in [28].

5.2. An improved general cavity projection algorithm

For the volume integrals with discontinuous kernel, there is an intersection region between the spherical surface and the boundary of element if a larger radius of the sphere is taken. How to match the projection points to fill the surface-gap appropriately is of crucial importance for ultimate patch generation. The general cavity projection algorithm has been successfully applied to the evaluation of nearly singular domain integrals, which is determined by the location types of cavity points and the number of cavity root faces in vicinity of the candidate cavity point. Note that there are some differences in the BTSM implementation for singular domain integrals. An improved general projection algorithm for both linear and curved elements is proposed on the basis of literature [26].

According to [26], the points in the ultimate refinement structure can be categorized into four types: *corner points, frame points, boundary points* and *interior points*. Several boundary matching types in Fig. 17 have been established based on the situation where the cavity points fall on various locations of element. The projection source point labeled P' indicates that the point which is closed to the source point P on the boundary of element. The point labeled A' is defined as the target projection point, which is obtained by projecting the cavity point Aalong the specified direction $\overrightarrow{P'A}$ to the characteristic boundary of sphere. The faces with purple lines are marked as a part of the cavity faces related to the candidate cavity point. For cases of the interior point or the boundary point that belongs to multiple cavity faces (see (a) and (b_2) in Fig. 17), and the corner point or the frame point whose adjacent cavity faces belong to all the root faces around the point (see (c_3) and (d_3) in Fig. 17), the target projection point A' is projected onto the characteristic boundary of sphere along the radial direction. For cases of the corner point whose adjacent cavity faces belong to a single root face (Fig. 17(c_1)), and the frame point whose adjacent cavity faces do not locate on any root face (Fig. 17(d_1)), the target projection point A' is projected onto the characteristic boundary of sphere along the root edge which is not adjacent to any cavity faces. For cases of the boundary point whose adjacent cavity faces do not locate on any root face (Fig. 17(b_1)), the corner point whose adjacent cavity faces belong to two root faces (Fig. 17(c_2)), and the frame point whose adjacent cavity faces belong to a single cavity root face (Fig. 17(d_2)), the target projection point A' is projected onto the characteristic boundary of sphere along the root face which is not coplanar with any cavity faces. After the projection of all cavity faces, the new layer of patches in the vicinity of spherical surfaces should be converted into well-shaped serendipity patches in order to approximate the spherical surface better and eliminate the gap between the sphere and the projection patches. An example of the improved general cavity projection algorithm for the projection of cavity points is depicted graphically in Fig. 18.

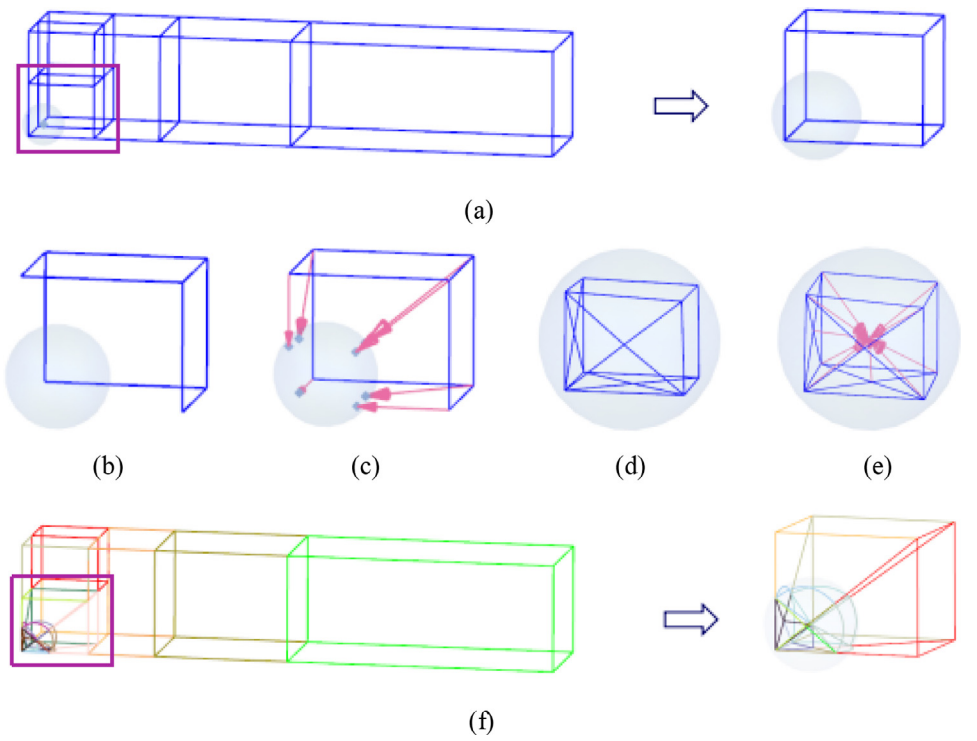

Fig. 18. Overall procedure of the improved general cavity projection algorithm: (a) ultimate refinement structure and the straddling sub-elements, (b) the outer projection cavity, (c) relative projection points of the outer projection cavity using the improved general cavity projection algorithm, (d) the inner projection cavity construction using the point insertion algorithm, (e) relative projection points of the inner projection cavity, (f) the resulting patch generation.

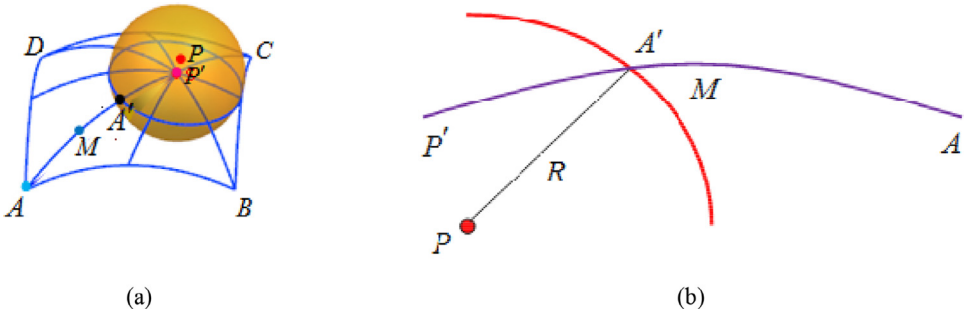

Fig. 19. The improved general projection algorithm based on the Newton iteration: (a) match the projection points on the curved boundary of element, (b) schematic of the Newton iteration for projection.

For boundary matching of the curved volume elements, the main dilemma is to accurately match the projection points on the curved boundary of element using the general projection algorithm. An improved general projection algorithm has been developed for curved elements based on the Newton iteration [29]. The proposed algorithm has the advantages of simplicity, feasibility and less iteration. Detailed illustration of the improved general cavity projection algorithm using Newton iteration is presented in Fig. 19.

The curved face *ABCD* is a root face of the prescribed volume element. If there are some cavity points along the boundary root edges of *ABCD*. The essence of the issue is to get the target projection points of the cavity points not only on the curved face *ABCD* but also on the spherical surface. The objective function of Newton iteration is defined by the intersection of a quadratic curve and the spherical surface, which can be expressed as

$$F(t) = |C(t) - O|^2 - R^2 \tag{2}$$

and the iterative sequence is given by

$$t_{k+1} = t_k - \frac{\left(\left|C(t_k) - O\right| - R\right)\left|C(t_k) - O\right|}{\left(C(t_k) - O\right) \cdot C'(t_k)} \tag{3}$$

where $C(t)$ is an arbitrary point on the quadratic curve, R is the radius of sphere, O is the center point of sphere, $|C(t) - O|$ denotes the distance from the point $C(t)$ to the center O, t_k and t_{k+1} are the parametric coordinates in steps k and $k + 1$, respectively.

For the projection of the cavity point A, we should first create a quadratic curve $\overline{AMP'}$ on the curved boundary face. The arbitrary point M on the curved boundary face is interpolated by A and P'. The objective function is minimized to obtain the accurate intersection point, viz., the target projection point A' in Fig. 19. Thus, a complex intersection problem is converted to the intersection between a quadratic curve and the boundary of spherical surface. An example in Fig. 20 illustrates the feasibility and advantages of this projection algorithm.

6. Numerical examples

In order to examine the applicability and stability of the BTSM for singular domain integrals, the element subdivision process was carried out for different types of elements. A comparison of the BTSM and the CSM for evaluation of singular domain integrals is given in this section. The convergence performance of the BTSM is demonstrated in Section 6.1. Several examples of different types of linear and curved elements are employed to verify the availability that the BTSM is applicable to evaluate the volume integrals with continuous or discontinuous kernels in Section 6.2 and Section 6.3, respectively. The continuous kernel and discontinuous kernel employed in the volume integrals can be

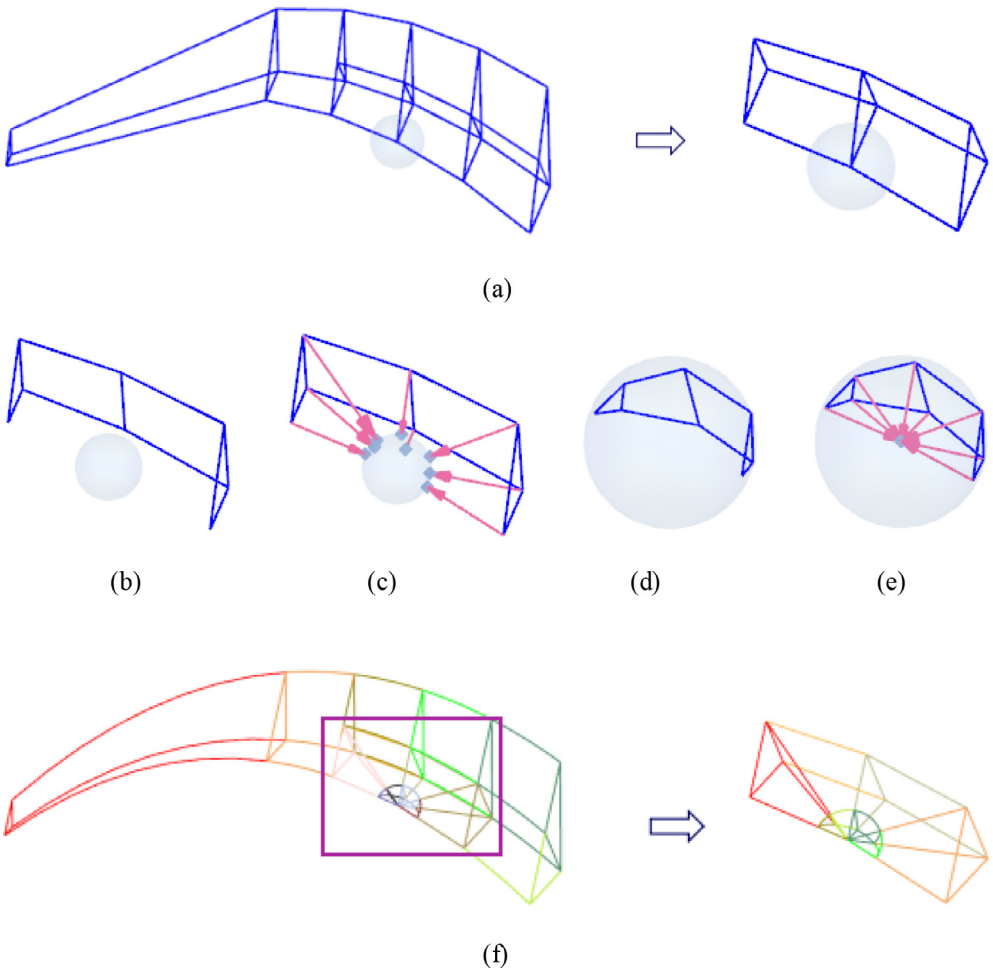

Fig. 20. Overall procedure of the improved general cavity projection algorithm for projection based on the Newton iteration: (a) ultimate refinement structure and the straddling sub-elements, (b) the outer projection cavity, (c) curved boundary matching based on the Newton iteration, (d)(e) the projection cavities and relative projection points, (f) the resulting patch generation.

respectively expressed as

$$I = \int_{\Omega} \frac{1}{4\pi r^2} N d\Omega \tag{4}$$

$$I = \begin{cases} \int_{\Omega} \frac{1}{r^2} N d\Omega & r \le 0.2 \\ \int_{\Omega} \frac{1}{4\pi r^2} N d\Omega & r > 0.2 \end{cases} \tag{5}$$

and the accuracy of the method is measured by using a relative error

$$\delta = \left| \frac{I_{(n)} - I_{(e)}}{I_{(e)}} \right| \tag{6}$$

where r is the distance from the source point to the field point, N is the arbitrary distributed function, $I_{(n)}$,$I_{(e)}$ denote the numerical and the exact results of singular domain integrals, respectively. The continuous and discontinuous kernels in Eqs. (4) and (5) are depicted graphically in Fig. 21.

6.1. Evaluation of convergence performance of the BTSM

To demonstrate the convergence performance of the proposed method, three examples for adaptive element subdivision created with the BTSM are provided. For the prescribed source point, the ultimate patch generation for singular domain integrals is unique. Different number of the integration points is employed to achieve the volume integrals with high accuracy. A comparison of convergence of the BTSM and the CSM for evaluation of singular domain integrals is also given.

6.1.1. Slender hexahedral element

The element subdivision of linear slender hexahedral element with the prescribed source point for singular domain integrals with continuous kernel in Eq. (4) is presented in Fig. 22. Unless otherwise mentioned, point coordinates of the linear slender hexahedral element in the Cartesian coordinate system are (1, 0, 0), (1, 0, 5), (1, 1, 5), (1, 1, 0), (0, 0, 0), (0, 0, 5), (0, 1, 5), (0, 1, 0). Numerical results in Table 1 clearly show the high accuracy of the BTSM compared to the CSM.

6.1.2. Slender tetrahedral element

The element subdivision of linear slender tetrahedral element with the prescribed source point is presented in Fig. 23 for singular domain integrals with continuous kernel in Eq. (4). Unless otherwise mentioned, point coordinates of the linear slender tetrahedral element in the Cartesian coordinate system are (−3, −3, −3), (0, 1, 0), (0, 0, 1), (1, 0, 0). Numerical results in Table 2 clearly show the high accuracy of the BTSM compared to the CSM.

6.1.3. Slender pentahedral element

The element subdivision of linear slender pentahedral element with the prescribed source point is presented in Fig. 24 for singular domain integrals with continuous kernel in Eq. (4). Unless otherwise mentioned, point coordinates of the linear slender pentahedral element in the Cartesian coordinate system are (0, 0.25, 0), (0, 0, 0), (0.25, 0, 0), (0, 1, 5), (0, 0, 5), (1, 0, 5). Numerical results in Table 3 clearly show the high accuracy of the BTSM compared to the CSM.

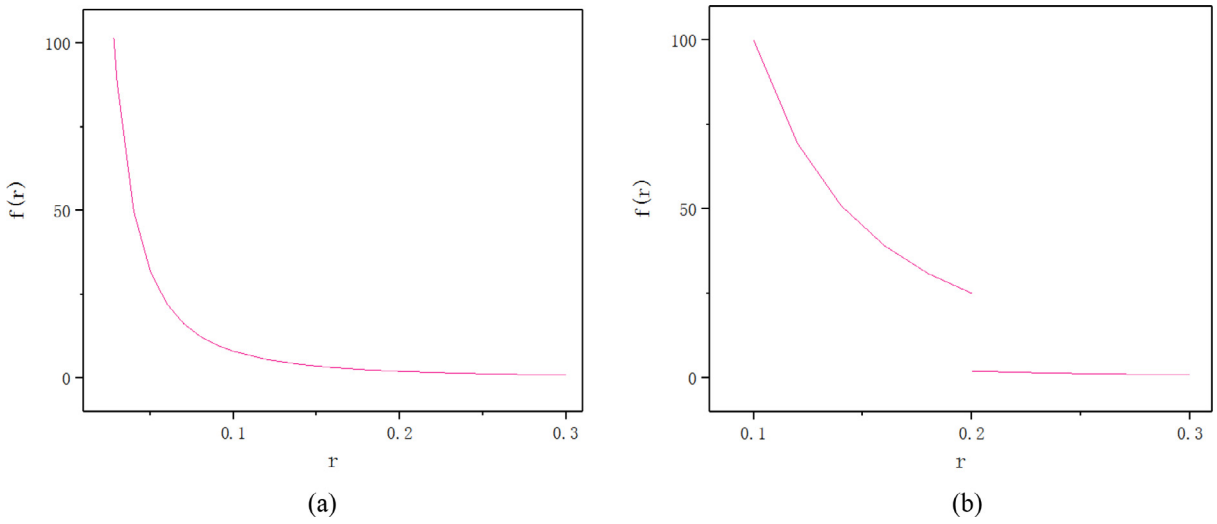

Fig. 21. The graph of the continuous and discontinuous kernel: (a) the continuous kernel, (b) the discontinuous kernel.

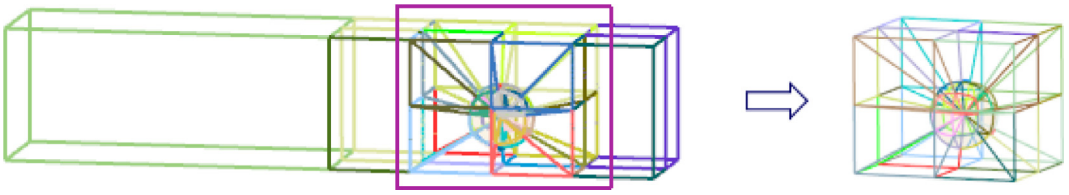

Fig. 22. The Cartesian coordinate of source point is (0.625, 0.375, 3.75).

Table 1
Numerical evaluation of singular domain integrals with continuous kernel for linear slender hexahedral element.

Volume element type	Source point	The total number of the integration points		Relative error	
		CSM	BTSM	CSM	BTSM
Linear slender hexahedral element	(0.625, 0.375, 3.75)	1296	898	8.62e−002	1.79e−003
		2058	1786	2.36e−002	1.87e−004
		4374	3954	3.95e−003	2.07e−005

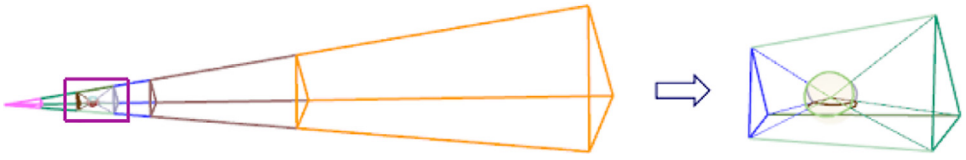

Fig. 23. The Cartesian coordinate of source point is (−2.5, −2.5, −2.5).

Table 2
Numerical evaluation of singular domain integrals with continuous kernel for linear slender tetrahedral element.

Volume element type	Source point	The total number of the integration points		Relative error	
		CSM	BTSM	CSM	BTSM
Linear slender tetrahedral element	(−2.5, −2.5, −2.5)	1372	936	7.83e−002	9.65e−003
		2916	2219	4.77e−002	8.95e−004
		4000	3380	1.62e−003	4.25e−005

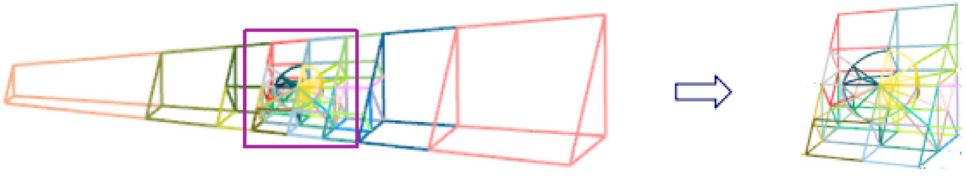

Fig. 24. The Cartesian coordinate of source point is (0.3125, 0. 3125, 2.5).

Table 3
Numerical evaluation of singular domain integrals with continuous kernel for linear slender pentahedral element.

Volume element type	Source point	The total number of the integration points		Relative error	
		CSM	BTSM	CSM	BTSM
Linear slender pentahedral element	(0.3125, 0. 3125, 2.5)	1458	1008	9.61e−002	9.29e−003
		3456	3119	6.19e−002	1.01e−005
		4394	3283	2.67e−003	2.31e−006

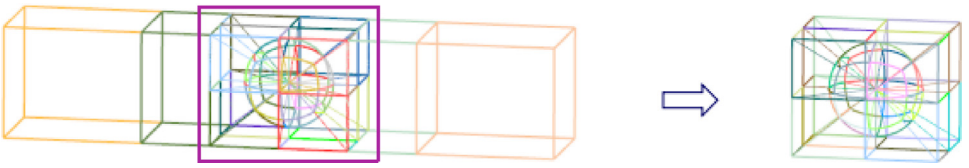

Fig. 25. The Cartesian coordinate of source point is (0.5, 0.5, 2.5).

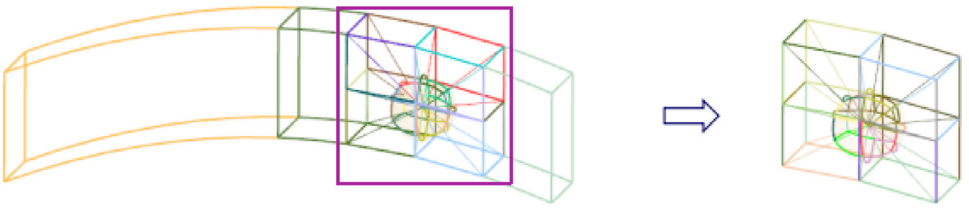

Fig. 26. The Cartesian coordinate of source point is (−0.6, −2.21, 0.375).

Table 4
Numerical evaluation of singular domain integrals with continuous kernel for linear slender hexahedral element.

Volume element type	Source point	The total number of the integration points		Relative error	
		CSM	BTSM	CSM	BTSM
Linear slender hexahedral element	(0.875, 0.125, 1.25)	3072	3024	6.58e−002	3.06e−005
	(0.5, 0.5, 2.5)	4374	3436	3.32e−002	6.01e−005
	(0.625, 0.375, 3.75)	4374	3954	3.95e−003	2.07e−005
	(0.5, 0.5, 5.0)	1715	1798	1.50e−003	6.25e−005

Table 5
Numerical evaluation of singular domain integrals with continuous kernel for quadratic slender hexahedral element.

Volume element type	Source point	The total number of the integration points		Relative error	
		CSM	BTSM	CSM	BTSM
Quadratic slender hexahedral element	(−1.9, −1.9, 0.125)	3072	3068	7.33e−002	1.95e−005
	(−1.04, −1.78, 0.5)	4374	3316	3.33e−002	5.78e−005
	(−0.6, −2.21, 0.375)	3072	2970	2.64e−002	7.65e−006
	(0.0, −2.17, 0.5)	1715	1774	3.74e−003	1.92e−005

6.2. Evaluation of singular domain integrals with continuous kernel

6.2.1. Slender hexahedral element

The element subdivision of linear and quadratic slender hexahedral element with arbitrary locations of the source point for singular domain integrals with continuous kernel is presented in Figs. 25 and 26. Unless otherwise mentioned, point coordinates of the quadratic slender hexahedral element in the Cartesian coordinate system are (1, 0, 0), (1, 0, 5), (1, 1, 5), (1, 1, 0), (0, 0, 0), (0, 0, 5), (0, 1, 5), (0, 1, 0), (0.5, 0, 2.5), (1, 0.5, 5), (0.5, 1, 2.5), (1, 0.5, 0), (−0.5, 0, 2.5), (0, 0.5, 5), (−0.5, 1, 2.5), (0, 0.5, 0), (0.5, 0, 0), (0.5, 0, 5), (0.5, 1, 5), (0.5, 1, 0). Numerical results in Tables 4 and 5 clearly show the high accuracy of the BTSM compared to the CSM.

6.2.2. Slender tetrahedral element

The element subdivision of linear and quadratic slender tetrahedral element with arbitrary locations of the source point is presented in Figs. 27 and 28 for singular domain integrals with continuous kernel. Unless otherwise mentioned, point coordinates of the quadratic slender tetrahedral element in the Cartesian coordinate system are (−3, −3, −3), (0, 1, 0), (0, 0, 1), (1, 0, 0), (−0.5, −1, −1.5), (−0.5, −1.5, −1), (0, −1.5, −1.5), (0, 0.5, 0.5), (0.5, 0, 0.5), (0.5, 0.5, 0). Numerical results in Tables 6 and 7 clearly show the high accuracy of the BTSM compared to the CSM.

6.2.3. Slender pentahedral element

The element subdivision of linear and quadratic slender pentahedral element with arbitrary locations of the source point is presented in Figs. 29 and 30 for singular domain integrals with continuous kernel. Unless otherwise mentioned, point coordinates of the quadratic slender pentahedral element in the Cartesian coordinate system are (0, 0.25, 0), (0, 0, 0), (0.25, 0, 0), (0, 1, 5), (0, 0, 5), (1, 0, 5), (0, 0.125, 0), (0.125, 0, 0), (0.125, 0.125, 0), (0, 0.5, 5), (0.5, 0, 5), (0.5, 0.5, 5), (1, 0.625, 2.5), (1, 0, 2.5), (1.625, 0, 2.5). Numerical results in Tables 8 and 9 clearly show the high accuracy of the BTSM compared to the CSM.

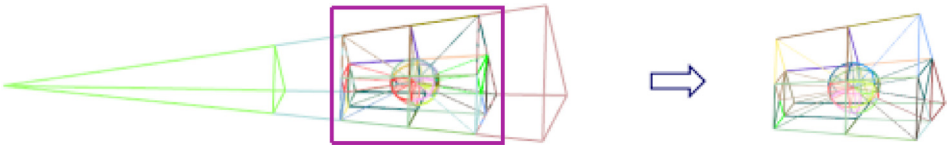

Fig. 27. The Cartesian coordinate of source point is (−0.5, −0.5, −0.5).

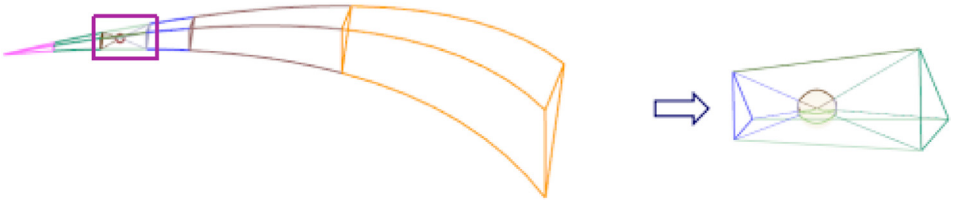

Fig. 28. The Cartesian coordinate of source point is (−2.0, −2.5, −2.5).

Table 6
Numerical evaluation of singular domain integrals with continuous kernel for linear slender tetrahedral element.

Volume element type	Source point	The total number of the integration points		Relative error	
		CSM	BTSM	CSM	BTSM
Linear slender tetrahedral element	(−2.5, −2.5, −2.5)	4000	3380	1.62e−003	4.25e−005
	(−2.0, −2.0, −2.0)	4000	3589	6.25e−002	4.59e−005
	(−0.5, −0.5, −0.5)	4000	3583	2.12e−002	7.66e−005
	(−2.4, −2.3, −2.3)	2187	1352	9.26e−002	3.15e−004

Table 7
Numerical evaluation of singular domain integrals for quadratic slender tetrahedral element.

Volume element type	Source point	The total number of the integration points		Relative error	
		CSM	BTSM	CSM	BTSM
Quadratic slender tetrahedral element	(−2.0, −2.5, −2.5)	4000	3602	6.47e−002	3.72e−005
	(−1.16, −2.0, −2.0)	4000	3372	3.05e−002	1.48e−005
	(0.25, −0.5, −0.5)	2916	2719	6.94e−002	3.03e−005
	(−1.76, −2.3, −2.3)	2187	1621	8.18e−002	9.92e−005

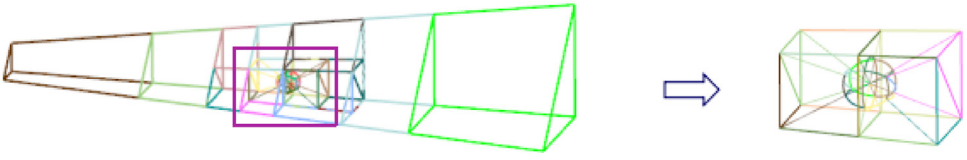

Fig. 29. The Cartesian coordinate of source point is (0.156, 0.156, 2.5).

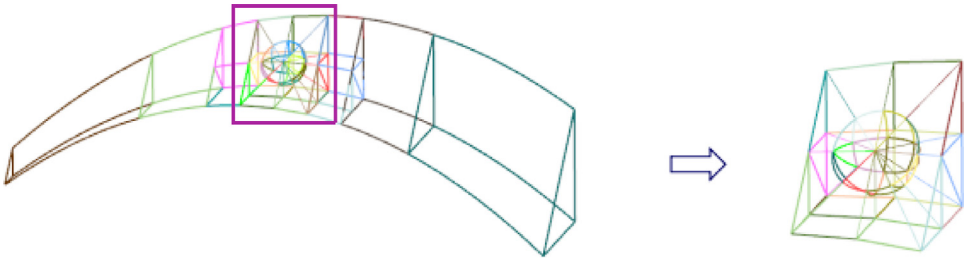

Fig. 30. The Cartesian coordinate of source point is (1.31, 0.31, 2.5).

Table 8
Numerical evaluation of singular domain integrals with continuous kernel for linear slender pentahedral element.

Volume element type	Source point	The total number of the integration points		Relative error	
		CSM	BTSM	CSM	BTSM
Linear slender pentahedral element	(0.175, 0.13, 1.25)	3993	3206	2.91e−002	2.18e−004
	(0.156, 0.156, 2.5)	3000	2835	7.31e−002	5.26e−004
	(0.3125, 0.3125, 2.5)	3456	3119	6.19e−002	1.01e−005
	(0.24, 0.325, 3.75)	3993	3541	5.01e−002	2.92e−005

Table 9
Numerical evaluation of singular domain integrals with continuous kernel for quadratic slender pentahedral element.

Volume element type	Source point	The total number of the integration points		Relative error	
		CSM	BTSM	CSM	BTSM
Quadratic slender pentahedral element	(0.925, 0.13, 1.25)	3993	3267	2.69e−002	2.79e−004
	(1.156, 0.156, 2.5)	3000	2523	6.27e−002	7.35e−005
	(1.31, 0.31, 2.5)	2662	2686	7.20e−002	5.87e−004
	(0.99, 0.325, 3.75)	3993	3169	5.22e−002	3.49e−005

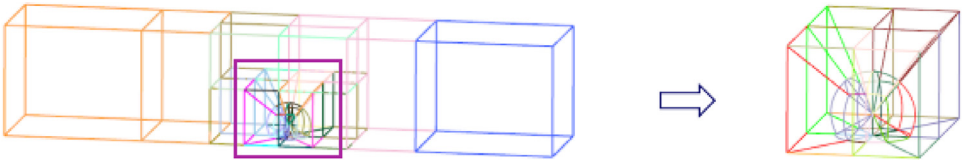

Fig. 31. The Cartesian coordinate of source point is (0.9, 0.5, 2.5).

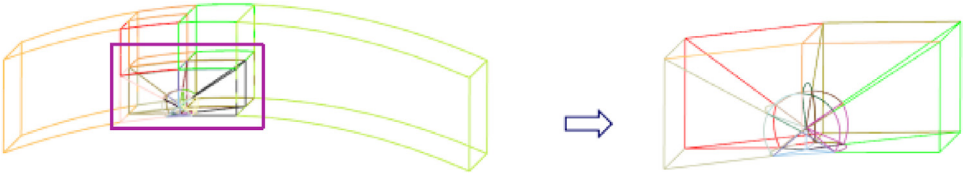

Fig. 32. The Cartesian coordinate of source point is (−1.66, −2.16, 0.1).

Table 10
Numerical evaluation of singular domain integrals with discontinuous kernel for linear slender hexahedral element.

Volume element type	Source point	The total number of the integration points		Relative error	
		CSM	BTSM	CSM	BTSM
Linear slender hexahedral element	(0.975, 0.025, 0.125)	3072	2964	2.91e−001	6.40e−004
	(0.9, 0.1, 1.875)	4374	3522	3.52e−002	6.35e−005
	(0.9, 0.5, 2.5)	4374	3300	4.96e−002	6.64e−005
	(0.75, 0.25, 2.5)	4374	3076	5.73e−002	5.47e−004

Table 11
Numerical evaluation of singular domain integrals with discontinuous kernel for quadratic slender hexahedral element.

Volume element type	Source point	The total number of the integration points		Relative error	
		CSM	BTSM	CSM	BTSM
Quadratic slender hexahedral element	(−2.43, −1.5, 0.025)	4374	4322	7.15e−002	2.12e−004
	(−1.66, −2.16, 0.1)	3072	3016	1.73e−002	3.09e−005
	(−1.04, −1.78, 0.1)	4374	4336	5.26e−002	3.25e−005
	(−1.25, −2.14, 0.25)	4374	4094	6.25e−002	8.82e−005

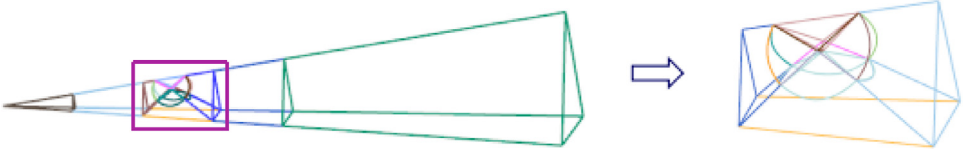

Fig. 33. The Cartesian coordinate of source point is (−1.9, −2.05, −2.05).

6.3. Evaluation of singular domain integrals with discontinuous kernel

6.3.1. Slender hexahedral element

The element subdivision of linear and quadratic slender hexahedral element with arbitrary locations of the source point is presented in Figs. 31 and 32 for singular domain integrals with discontinuous kernel. Numerical results in Tables 10 and 11 clearly show the high accuracy of the BTSM compared to the CSM.

6.3.2. Slender tetrahedral element

The element subdivision of linear and quadratic slender tetrahedral element with arbitrary locations of the source point is presented in Figs. 33 and 34 for singular domain integrals with discontinuous kernel. Numerical results in Tables 12 and 13 clearly show the high accuracy of the BTSM compared to the CSM.

6.3.3. Slender pentahedral element

The element subdivision of linear and quadratic slender pentahedral element with arbitrary locations of the source point is presented in Figs. 35 and 36 for singular domain integrals with discontinuous kernel. Numerical results in Tables 14 and 15 clearly show the high accuracy of the BTSM compared to the CSM.

As is illustrated in Figs. 22–24, it is clearly seen that high-quality patch generation for both linear and curved elements can be achieved in a fully automated manner and the serendipity patches are well matched to the characteristic boundary of sphere. Numerical results presented in

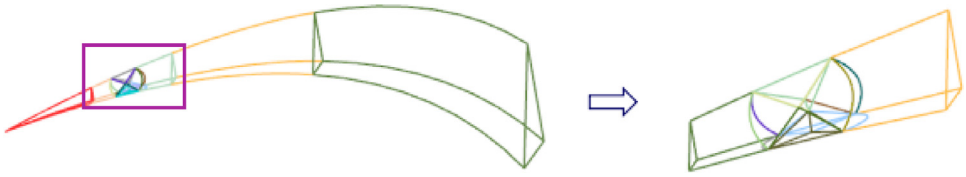

Fig. 34. The Cartesian coordinate of source point is (−1.8, −2.4, −2.4).

Table 12
Numerical evaluation of singular domain integrals with discontinuous kernel for linear slender tetrahedral element.

Volume element type	Source point	The total number of the integration points		Relative error	
		CSM	BTSM	CSM	BTSM
Linear slender tetrahedral element	(−2.4, −2.4, −2.4)	2048	1215	2.38e−001	5.08e−004
	(−0.5, −0.5, −0.5)	4000	3463	3.36e−002	3.25e−005
	(−0.5, −0.25, −0.25)	4000	2850	2.71e−002	1.21e−004
	(−1.9, −2.05, −2.05)	2048	1756	4.01e−001	2.09e−005

Table 13
Numerical evaluation of singular domain integrals with discontinuous kernel for quadratic slender tetrahedral element.

Volume element type	Source point	The total number of the integration points		Relative error	
		CSM	BTSM	CSM	BTSM
Quadratic slender tetrahedral element	(−1.8, −2.4, −2.4)	2048	1218	3.07e−001	4.46e−004
	(0.25, −0.5, −0.5)	4000	3132	4.26e−002	5.40e−004
	(0.14, −0.25, −0.25)	4000	3557	1.70e−002	2.45e−004
	(−1.06, −2.05, −2.05)	2048	1854	2.93e−001	7.57e−004

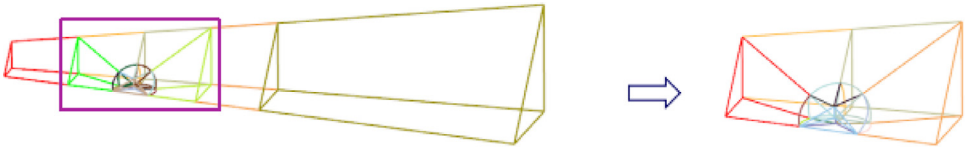

Fig. 35. The Cartesian coordinate of source point is (0.043, 0.35, 1.25).

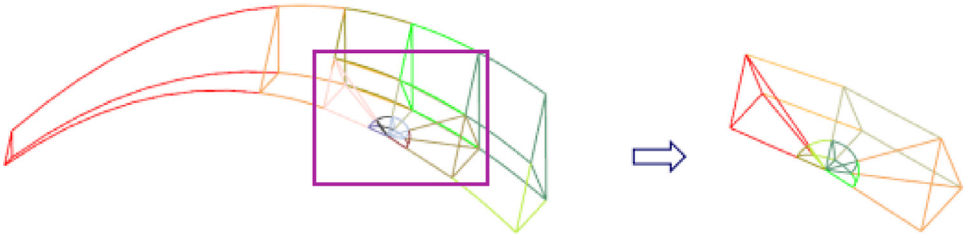

Fig. 36. The Cartesian coordinate of source point is (0.75, 0.8, 3.75).

Table 14
Numerical evaluation of singular domain integrals with discontinuous kernel for linear slender pentahedral element.

Volume element type	Source point	The total number of the integration points		Relative error	
		CSM	BTSM	CSM	BTSM
Linear slender pentahedral element	(0.013, 0.24, 0.125)	3000	2888	2.41e−001	4.96e−005
	(0.043, 0.35, 1.25)	3000	2892	2.54e−001	7.30e−007
	(0.406, 0.243, 3.75)	3000	2882	2.97e−002	3.83e−006
	(0.0, 0.81, 3.75)	2197	2182	3.15e−002	1.41e−005

Table 15
Numerical evaluation of singular domain integrals with discontinuous kernel for quadratic slender pentahedral element.

Volume element type	Source point	The total number of the integration points		Relative error	
		CSM	BTSM	CSM	BTSM
Quadratic slender pentahedral element	(0.11, 0.24, 0.125)	3000	2541	3.24e−001	1.31e−004
	(0.8, 0.35, 1.25)	2187	1847	4.92e−001	1.29e−004
	(1.156, 0.24, 3.75)	3000	2935	2.88e−002	7.43e−007
	(0.75, 0.8, 3.75)	3375	3004	9.79e−003	5.46e−007

Tables 1–3 are evaluated with the increasing number of the integration points, which verify that the BTSM has higher accuracy and better convergence than the CSM. Obviously, it can be observed from Figs. 25–36 that the BTSM is applicable to evaluate singular domain integrals with continuous or discontinuous kernels. Even with the distorted elements, the accuracy and convergence of the BTSM is still acceptable, which further demonstrates the validity of the proposed method. Numerical results presented in Tables 4–15 also demonstrate that the BTSM is reliable and stable for the volume integrals of different types of elements with arbitrary locations of the source point. It is appealing that the BTSM for singular domain integrals exhibits high accuracy and excellent robustness behavior.

7. Conclusions and future work

A new element subdivision method based on the binary tree for evaluation of singular domain integrals is presented. One of the main difficulties encountered in evaluation of volume integrals with discontinuous kernel, we introduce the BTSM for different types of element subdivision. The BTSM is applicable to linear and curved volume elements of arbitrary shape and high-quality patch generation can be achieved in a fully automated manner. Besides, a new type of face-tree data structure and several adaptive refinement techniques are added in this paper. For curved boundary matching, an improved general projection algorithm based on Newton iteration also has been proposed. With the distinct feature that the single binary-tree data structure can efficiently handle volume element subdivision, the BTSM is flexible and convenient to be applied in the BEM implementation.

Numerical results are presented for different types of volume elements comparing the CSM and the BTSM. The BTSM exhibits high accuracy and excellent robustness behavior. Compared to the CSM, significantly better accuracy can be achieved by the BTSM for singular domain integrals. Recently, in the efforts to improve the performance of the volume integrals, the spline rules for integration were coupled successfully to BEM and have been achieved remarkable progress. Based on the prominent properties of the spline rules for integration [30], further research work is in process by our team, which will substantially relieve the burden of the integration with extensive unnecessary integration points. In future work, we also plan on developing the BTSM to evaluate the volume integrals with kernels which contain multiple discontinuous points.

Acknowledgments

This work was supported by the National Natural Science Foundation of China (No. 11772125).

References

[1] Jaswon MA. Integral equation methods in potential theory. Proc R Soc Ser A 1963;275:23–32.
[2] Zhang JM, Qin XY, Han X, Li GY. A boundary face method for potential problems in three dimensions. Int J Numer Meth Eng 2009;80(3):320–37.
[3] Zhang JM, Chi B, Lin W, et al. A dual interpolation boundary face method for three--dimensional potential problems. Int J Heat Mass Transf 2019;140:862–76.
[4] Zhongrong N, Xiuxi W, et al. A novel boundary integral equation method for linear elasticity—natural boundary integral equation. Acta Mech Solida Sin 2001;14(1):1–10.
[5] Liu YJ. Analysis of shell-like structures by the boundary element method based on 3-D elasticity: formulation and verification. Int J Numer Meth Eng 1998;41(3):541–58.
[6] Zhang JM, Zhong Y, Dong Y, et al. Expanding element interpolation method for analysis of thin-walled structures. Eng Anal Bound Elem 2018;86:82–8.
[7] Dong C Y, Yang X, Pan E. Analysis of cracked transversely isotropic and inhomogeneous solids by a special BIE formulation. Eng Anal Bound Elem 2011;35(2):200–6.
[8] ChenHaibo Singular solutions of anisotropic plate with an elliptical hole or a crack. Acta Mech Solida Sin 2005;18(2):130–41.
[9] Peake M J, Trevelyan J, Coates G. Extended isogeometric boundary element method (XIBEM) for three-dimensional medium-wave acoustic scattering problems. Comput Methods Appl Mech Eng 2015;284:762–80.
[10] Chen JT, Lee YT, Lin YJ. Analysis of multiple-spheres radiation and scattering problems by using null-field integral equations. Appl Acoust 2010;71:690–700.
[11] Zhou F, Li Y, et al. A time step amplification method in boundary face method for transient heat conduction. Int J Heat Mass Transf 2015;84:671–9.
[12] Ma H, Yin F, Qin Q H. Performance and numerical behavior of the second-order scheme of precise time-step integration for transient dynamic analysis. Numer Methods Partial Differ Equ 2007;23(6):1301–20.
[13] Davies TG, Gao XW. Three-dimensional elasto-plastic analysis via the boundary element method. Comput Geotech 2006;33(3):145–54.
[14] Ochiai Y, Sladek V. Numerical treatment of domain integrals without internal cells in three-dimensional BIEM formulations. Comput Model Eng Sci 2004;6(6):525–36.
[15] Hematiyan MR, Khosravifard A, Bui TQ. Efficient evaluation of weakly/strongly singular domain integrals in the BEM using a singular nodal integration method. Eng Anal Bound Elem 2013;37(4):691–8.
[16] Gao XW. The radial integration method for evaluation of domain integrals with boundary-only discretization. Eng Anal Bound Elem 2002;26(10):905–16.
[17] Ingber MS, Mammoli AA, Brown MJ. A comparison of domain integral evaluation techniques for boundary element methods. Int J Numer Methods Eng 2001;52(4):417–32.
[18] Dong Y, Lu C, Li Y, et al. Accurate numerical evaluation of domain integrals in 3D boundary element method for transient heat conduction problem. Eng Anal Bound Elem 2015;60:89–94.
[19] Dong Y, Zhang J, Xie G, et al. A general algorithm for the numerical evaluation of domain integrals in 3D boundary element method for transient heat conduction. Eng Anal Bound Elem 2015;51:30–6.
[20] Rannou J, Gravouil A, Baïetto-Dubourg M C. A local multigrid X-FEM strategy for 3-D crack propagation. Int J Numer Methods Eng 2009;77(4):581–600.
[21] Klees R. Numerical calculation of weakly singular surface integrals. J Geodesy 1996;70(11):781–97.
[22] Tanaka M, Zhang JM, Matsumoto T. Boundary-type meshless solution of potential problems: comparison between singular and regular formulations in hybrid BNM transactions of JASCOME. J Bound Element Methods 2003;20:21–6.
[23] Zhang JM, Lu C, Zhang X, et al. An adaptive element subdivision method for evaluation of weakly singular integrals in 3D BEM. Eng Anal Bound Elem 2015;51:213–19.
[24] Bentley JL. Multidimensional binary search trees used for associative searching. Commun ACM 1975;18(9):509–17.
[25] Hammer PC, Stroud AH. Numerical integration over simplexes. Math Tables Other Aids Comput 1956;10(55):137–9.
[26] Zhang JM, Chi B, Singh KM, et al. A binary-tree element subdivision method for evaluation of nearly singular domain integrals with continuous or discontinuous kernel. J Comput Appl Math 2019;362:22–40.
[27] Kwak DY, Im YT. Remeshing for metal forming simulations—part II: three-dimensional hexahedral mesh generation. Int J Numer Methods Eng 2002;53(11):2501–28.
[28] Stroud A.H. Approximate calculation of multiple integrals. 1971.
[29] Kelley CT. Iterative methods for optimization. Society for Industrial and Applied Mathematics; 1999.
[30] Barton M, Calo VM. Optimal quadrature rules for odd-degree spline spaces and their application to tensor-product-based isogeometric analysis. Comput Methods Appl Mech Eng 2016;305:217–40.